



HAL
open science

Influence of interlayer dwell time on the microstructure of Inconel 718 Laser Cladded components

Camille Guévenoux, Simon Hallais, Alexandre Charles, Eric Charkaluk,
Andrei Constantinescu

► **To cite this version:**

Camille Guévenoux, Simon Hallais, Alexandre Charles, Eric Charkaluk, Andrei Constantinescu. Influence of interlayer dwell time on the microstructure of Inconel 718 Laser Cladded components. *Optics and Laser Technology*, 2020, 128, pp.106218. 10.1016/j.optlastec.2020.106218 . hal-02517596

HAL Id: hal-02517596

<https://hal.science/hal-02517596>

Submitted on 24 Mar 2020

HAL is a multi-disciplinary open access archive for the deposit and dissemination of scientific research documents, whether they are published or not. The documents may come from teaching and research institutions in France or abroad, or from public or private research centers.

L'archive ouverte pluridisciplinaire **HAL**, est destinée au dépôt et à la diffusion de documents scientifiques de niveau recherche, publiés ou non, émanant des établissements d'enseignement et de recherche français ou étrangers, des laboratoires publics ou privés.

Influence of interlayer dwell time on the microstructure of Inconel 718 Laser Cladded components

Camille Guévenoux^{a,b}, Simon Hallais^a, Alexandre Charles^b, Eric Charkaluk^a, Andrei Constantinescu^a

^aLaboratoire de Mécanique des Solides, École polytechnique, Institut Polytechnique de Paris, CNRS, Palaiseau, France
^bSafran Tech, Magny-les-Hameaux, France

Abstract

Laser Cladding is one of the leading additive manufacturing technologies enabling the repair of metallic components. Their fatigue reliability depends directly on the material microstructure and consequently on the process parameters. This study highlights the influence of the interlayer dwell time on single-track walls for Inconel 718 repaired components. EBSD analyses show that dwell time both reduces grain size and creates a textural stretch of the microstructure. An optimal dwell time between the writing of successive layers can then be introduced to target a specified microstructure gradient at the interface between the original part and the repaired deposit.

Keywords: Additive manufacturing, Direct Laser Deposition, Electron BackScattering Diffraction (EBSD), Nickel alloys, microstructural gradient.

1. Introduction

The manufacturing of structural components out of technological alloys comes with a high cost and consequently, repair of defects or wear is a major asset for industry [1]. Within the novel technologies, Laser Cladding, also known as Direct Energy Deposition, is an emerging leader. The energy input in cladding is spatially localised and the heat affected zone smaller when compared with other repair processes [2–4]. In Laser Cladding repaired components, an interface with a microstructural gradient is created between the substrate and the cladded zone. It conditions the cohesion and the lifetime of repaired part [5, 6].

The process parameters, together with the particular geometry of the components, control the heat input, the melt pool shape and the spatial temperature gradients and cooling rates which condition the material microstructure. A material volume can be submitted to several solidification-remelt cycles with the printing of the above layers, depending of the melt pool depth and shape which can be quite complex as exhibited experimentally by Biegler *et al.* in [7]. The material also experiences annealing afterwards as the part stays at high temperatures until the end of the process [8, 9].

Many process parameters that have an impact on the process thermal history and consequently on the microstructure and mechanical properties of the final part have been widely investigated in the literature: laser speed and power or powder mass flow [10–14], lasing strategy [12, 15–19], laser spot characteristics [20] etc...

However, fewer works have focused on the influence of an inter-layer dwell time. It is indeed possible to wait between the printing of several layers, allowing the part to cool down during the process, completely changing the process thermal history as highlighted by Heigel *et al.* in [21] and Lei *et al.* in [8].

This will have a first impact on distortions occurring during the process and on final residual stresses. According to Denlinger *et al.*, dwell time increases distortion and residual stresses for Ti-6Al-4V whereas, for Inconel 625, dwell time decreases them. This experimental fact was confirmed by Heigel *et al.* for Ti-6Al-4V [21].

Other contributions have focused on different impacts of dwell time. In [22], Foster *et al.* studied both Inconel 625 and Ti-6Al-4V in terms of microstructure, hardness and mechanical behavior, their results are the following. Vickers' microhardness and the yield and tensile strengths increase with the addition of an inter-layer dwell time for both alloys. For Inconel 625, adding some dwell time decreases the secondary dendrite arm spacing. For Ti-6Al-4V, increasing dwell time slightly

Email address: camille.guevenoux@polytechnique.edu
(Camille Guévenoux)

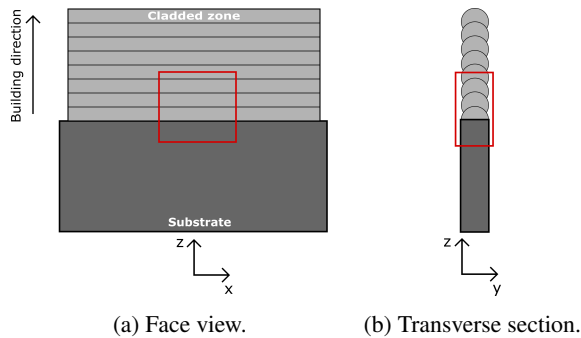


Figure 1: Geometry of the repaired specimen: a single-track wall is deposited by Laser Cladding on top of a wrought plate used as substrate.

decreases the alpha lath widths and also decreases the overall size of the prior beta grains. Kistler *et al.* who worked on Ti-6Al-4V have also found that dwell time increased hardness and they have shown that dwell time has no strong influence on HAZ depth, density of the deposited material [23].

The objective of this work is to complete the previous works quoted previously offering an in depth analysis of the microstructure of repaired Inconel 718 components in terms of grain morphology and orientation using EBSD analysis and taking under scrutiny the influence of dwell time on the interface and cladded area microstructure.

2. Material and methods

The experimental work was conducted on samples with simple geometry as described in Fig. 1. They consist of a thin plate acting as the substrate on top of which a single-track wall with a similar thickness is deposited by Laser Cladding as proposed initially in [24, 25].

The substrate is an Inconel 718 wrought plate with standard alloy composition described in [26]. Its thickness, length and height are respectively $e = 1.6\text{ mm}$, $L = 90\text{ mm}$ and $a = 20\text{ mm}$. The powder deposited by cladding is an Inconel 718 powder with particle size within $45 - 105\ \mu\text{m}$; it was manufactured by gas atomization by ARCAM [27].

The samples were manufactured on a Laser Cladding BeAM Mobile machine (see [28] for additional details). This machine is equipped with a coaxial nozzle including a powder jet, a local argon inerting and a fiber laser with wavelength 1070 nm offering a maximum power of 500 W and a spot diameter of 0.75 mm .

The process parameters were kept identical for all samples: laser speed ($2000\text{ mm/min} = 33.3\text{ mm/s}$), laser power (250 W), powder mass flow ($6\text{ g/min} = 100\text{ mg/s}$), vertical increment between two layers (0.2 mm), back and forth movement of the nozzle. Two types of walls were manufactured:

- (a) without any dwell time;
- (b) with a 10-second dwell time between two successive layers.

The dwell time increases the time between two successive depositions at a given spatial point. In the present experiment, the laser path takes $L/v = 2.7\text{ s}$ and therefore a dwell time of 10 seconds is significant since it almost multiplies by a factor 5 the cooling time of a material point between two depositions.

No heat treatment was applied to the samples after manufacturing.

The samples were water-jet cut to reveal the transverse section of the bi-material wall. No warping was recorded indicating that the residual stresses induced by manufacturing were kept at a reasonable level, below the buckling or plasticity threshold.

To conduct the EBSD analyses, the samples surface was mechanically polished up to $1\ \mu\text{m}$ before ion polishing in a *Gatan PECS II* machine. The samples were analyzed on two planes: face view and transverse section as displayed in Fig. 1.

The Scanning Electron Microscope used in this study for EBSD analysis is a *FEI Quanta 600 FEG-ESEM*.

The EBSD maps were acquired using the *Aztec* software with a step size of $1\ \mu\text{m}$. The data was then analyzed with *Channel 5* software to plot EBSD maps. The identification of each grains was obtained after imposing a misorientation threshold of 10° .

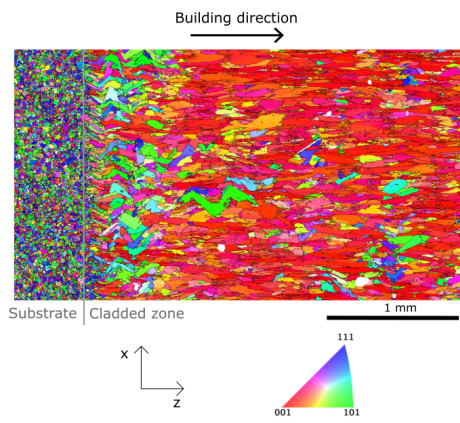
3. Results

The results of EBSD analyses are presented in Fig. 2 with Inverse Pole Figures along the building direction as colormap. The face views displayed in Fig. 2a and 2b are located at the center of the transverse sections as shown in Fig. 2c and 2d. This is due to the polishing of the faces that led to material removal of approximately $400\ \mu\text{m}$.

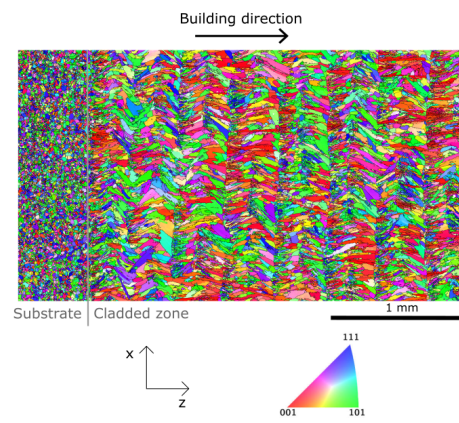
On all these microstructure maps, the substrate is composed of randomly oriented equiaxed grains with average size 15 microns. The cladded zone, however, exhibits a specific microstructure.

3.1. Plane view EBSD maps

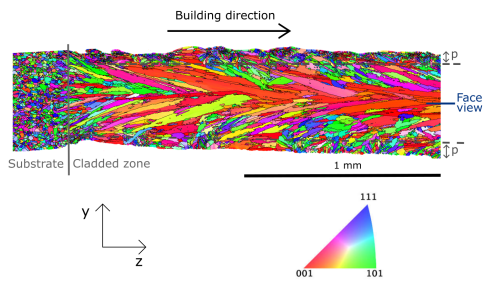
In Fig. 2a, the deposit material consists of large columnar grains, morphologically oriented along the



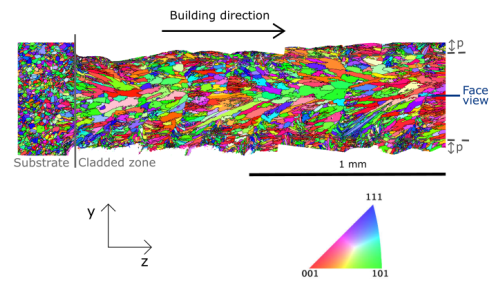
(a) Face view without dwell time.



(b) Face view with a 10-second dwell time.



(c) Transverse section without dwell time.



(d) Transverse section with a 10-second dwell time.

Figure 2: Comparison of the microstructures obtained without (a) (c) and with (b) (d) dwell time in term of Inverse Pole Figures along the building direction.

building direction, up to 1mm long, with an average aspect ratio close to 4. The microstructure is also strongly textured crystallographically: almost all grains have the crystal direction $\langle 100 \rangle$ oriented along the building direction. The process layers are not visible in this map. However, one can easily notice the transition zone between the substrate and the cladded region composed of smaller columnar grains forming a herringbone pattern following the layers.

With a 10-second dwell time, a completely different microstructure appears on Fig. 2b: the average grains aspect ratio is 2.5 and the morphological orientation of grains changes one layer over two with the printing direction. This herringbone pattern of columnar grains occupies the whole cladded deposit and allows to identify the successive written layers.

3.2. Transverse section EBSD maps

The EBSD maps in the transverse plane, displayed in Fig. 2c and 2d, reveal that the part of the walls near the surface is composed of small grains up to a depth of about 80 microns whereas in the central zone the grains are much larger. This is explained by the different cooling mechanisms involved: at the surface, convection at the surface is dominant whereas in the heart of the wall, the main flux is driven by conduction along the height of the wall thanks to the substrate thermal pumping. A detailed discussion regarding this phenomenon will be provided further in Sect. 4.2.

In Fig. 2c, one can remark that the central part of the wall exhibits large and textured columnar grains crossing the layers. During manufacturing, large grains near the interface epitaxially grow on small substrate grains with an appropriate crystallographic orientation which corresponds to the $\langle 100 \rangle$ direction aligned with the building direction. The EBSD map in Fig. 2d outlines that an interlayer dwell time will conduct to smaller grains that remain confined to one layer.

The preceding EBSD analyses highlight the strong influence of dwell time on grain size morphology and orientation of the Inconel 718 cladded material. Moreover, it equally influences the microstructural gradient between the original part and the repaired area. Without dwell time, the cladded deposit is highly textured, consists of very large columnar grains crossing the layers and the microstructural gradient is pronounced with a short transition area. When dwell time is applied, the microstructural gradient is smoother, grains do not cross the layers which stay visible throughout the height of the wall.

4. Discussion

Let us analyze next the observed microstructural differences in terms of cooling rates, spatial gradients and the consequent solidification process.

4.1. Epitaxial grain growth along the thermal gradient

In face-centered cubic crystal, epitaxial grain growth occurs along the $\langle 100 \rangle$ crystallographic direction [29, 30]. At solidification, the grains with $\langle 100 \rangle$ direction aligned with the thermal gradient grow faster than other grains and therefore these grains will characterize the microstructure as explained in [15, 17, 30].

Using the notation of Debroy *et al.* [3], the thermal gradient in our structure is a three-dimensional vector:

$$\underline{\nabla T} = g_x \underline{e}_x + g_y \underline{e}_y + g_z \underline{e}_z \quad (1)$$

where $g_x = \frac{\partial T}{\partial x}$, $g_y = \frac{\partial T}{\partial y}$ and $g_z = \frac{\partial T}{\partial z}$.

Let us first analyze the central region of the wall. Here, due to symmetry the component g_y is negligible with respect to the other components g_x and g_z . Then, the norm G of the thermal gradient writes

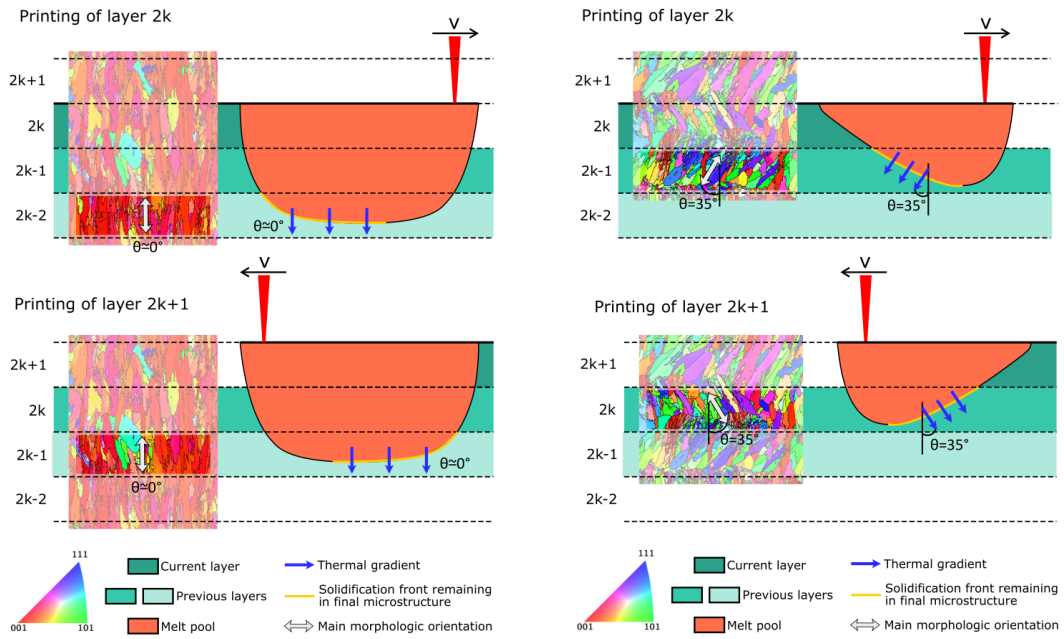
$$G = \|\underline{\nabla T}\| \simeq \sqrt{g_x^2 + g_z^2}. \quad (2)$$

The direction of $\underline{\nabla T}$ is determined by its angle θ verifying

$$\tan \theta = \frac{g_x}{g_z} \quad (3)$$

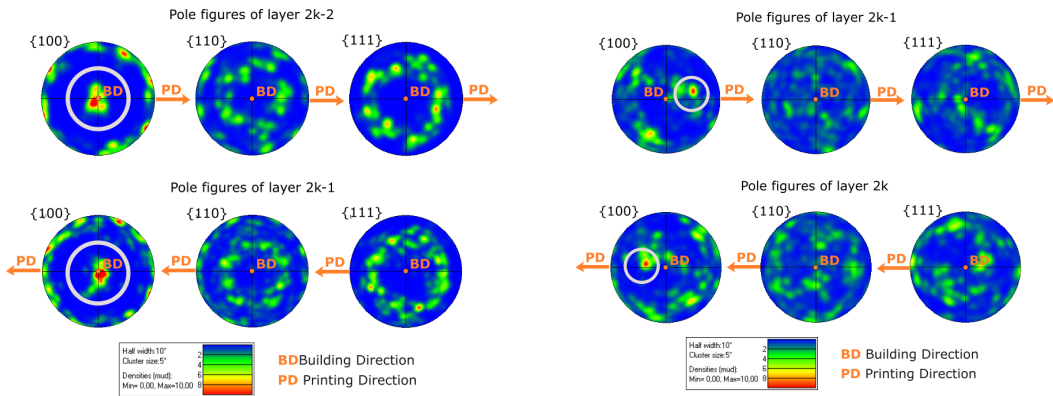
When a dwell time between the deposition of two successive layers is introduced, the wall has enough time to cool and the melt pool keeps its steady state shape during manufacturing. Due to the back and forth lasing strategy, the thermal gradient direction, which is the preferential grain growth direction, changes between two successive layers. It results in an herringbone pattern observed several times in the literature for additive manufacturing microstructure [12, 17]. The morphologic grain orientation was measured on the EBSD and it corresponds to a mean angle close to 35° with the z direction. Due to epitaxial growth, the grain elongation direction should coincide with $\langle 100 \rangle$ crystallographic direction [30]. This is confirmed by the pole figures shown in Fig. 3d where the majority of grains show a direction $\langle 100 \rangle$ forming a 35° angle with the building direction.

Consequently, on this specimen, the approximate direction of the thermal gradient on the melt pool boundary is provided by the resulting microstructure and allows us to draw schematically the melt pool shape for this manufacturing conditions on Fig. 3b. The angle θ



(a) No dwell time.

(b) With a 10-second dwell time.



(c) No dwell time.

(d) With a 10-second dwell time.

Figure 3: Schematic view of the melt pool shape and direction of principal thermal gradient driving solidification using inverse pole figure regarding the building direction (a) and (b) and pole figures (c) and (d). On the left, (a) and (c), without dwell time, the melt pool is large and deep and the thermal gradient is almost vertical; on the right, (d) and (d), with dwell time, the melt pool is smaller and the solidification front is inclined at an angle close to 35° to the building direction.

describe in Eq. 3 is 35° giving a ratio of thermal gradient components $g_x/g_z = \tan \theta \approx 0.7$.

Authors in [15, 17] mention that a back and forth laser strategy alters the growth direction of the primary dendrites in each layer by 90° with respect to the growth direction of primary dendrites of previous layer. Indeed, the microstructure grows by minimizing the solidification energy selecting one of the two following competitive phenomena: the growth of dendrites, whose secondary arm in the below layer can become the first arm in the above layer, and the germination of new crystals. In our case, it was apparently less costly for grains to grow aligned with the thermal gradient than to follow the orientation of the dendrites.

In the absence of dwell time, the average wall temperature increases. This phenomenon was reported by Heigel *et al.* in [21] on a similar geometry. They printed Ti-6Al-4V single-bead walls about 40mm long without dwell time or with a 20-second dwell time. Thermocouple measurements have shown that without dwell time, the average wall temperature was 600°C and with a 20-second dwell time, it was only 150°C . This important change in the thermal field explains why applying dwell time can completely change solidification conditions.

Without dwell time during manufacturing, the pattern of the layers disappears in favor of larger grains formed by epitaxy and crossing the layer boundaries with a main morphologic orientation and crystallographic direction $\langle 100 \rangle$ aligned with the building direction as exhibited in Fig. 2a and 3c. Similar microstructures were equally reported in [12, 31, 32] for high-power process parameters.

In this regime, the final microstructure indicates that the thermal gradient is then practically vertical (the angle θ of Eq. 3 is close to 0°) and that the melt pool frontier should then be almost horizontal as shown in the scheme of Fig. 3a. This demonstrates that, when no dwell time is applied, the global increase of temperature affects differently the thermal gradient components and that in this case g_x becomes negligible compared to g_z . Using Eq. 2, one finally gets in $G \approx g_z$.

It is important to highlight that the melt pool shapes drawn in Fig. 3 are only indicative and based on the main thermal gradient direction. However, melt pool does not necessarily exhibit a convex shape. In laser bed additive manufacturing process, for high energy parameters (high laser power or slow laser speed), the keyhole phenomenon well-known in welding can occur [33, 34]. When a massive amount of energy is imposed on a small area, the melt pool becomes narrow and deep which

can lead to important solidification defects [35]. Non convex melt pool shape were also reported with Laser Cladding by Biegler *et al.* [7].

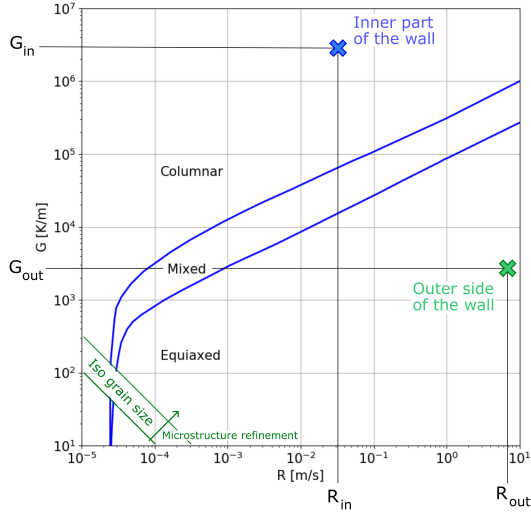
4.2. Convection and conduction cooling mechanisms

Let us further analyze the results using a classical solidification map to provide explanations regarding the difference between the inner part of the wall and its surface. This experimental log-log map displayed in Fig. 4a represents solidification regimes (columnar, mixed or equiaxed microstructure) with respect to thermal gradient G and liquid/solid interface velocity R [36].

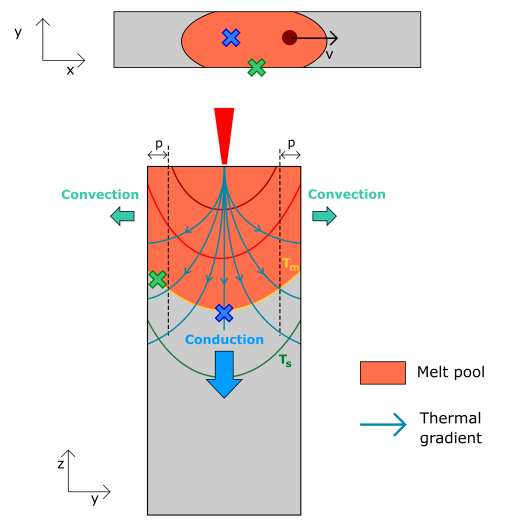
During manufacturing, far from the edges of the wall, the temperature reaches a steady state regime. The interface velocity in the kernel of the wall, R_{in} , is close to the laser speed $v = 2000 \text{ mm/min} = 3.33 \cdot 10^{-2} \text{ m/s}$, whether we add dwell time or not [37]. Various numerical studies conducted in the literature [3, 37, 38] agrees that the thermal gradient at solidification far from the edges G_{in} is between 10^6 and 10^7 K/m depending on process parameters. The value of (R_{in}, G_{in}) provide an approximate position in the solidification map of Fig. 4a for the inner part of the wall where cooling is ensured by conduction: it is located in the columnar domain, which matches the observation made on the EBSD.

Let us now investigate the convection mechanism on the surface of the single-track wall. Convection is usually not the main cooling mechanism in DED and is frequently considered negligible in front of conduction [3]. However, neglecting it for thin wall geometries can lead to errors according to Michaleris in [39]. The EBSD analysis conducted on the transverse cut of our samples shows a thin surface layer with a different microstructure. The layer is only 0.08 mm thick, so if it belonged to a massive component it would be indeed negligible. Nevertheless, on a thin geometry like the one considered in the article (laser bead and plate thickness of 0.8 mm) the surface layers compose one fifth of the overall thickness and can consequently play a part in the mechanical properties of the structure.

To understand why convection generates a different microstructure when compared with the one analyzed previously and generated by conduction, R_{out} and G_{out} , thermal gradient and interface velocity near the surface, need to be evaluated. Fig. 4b displays a schematic view of the isothermal lines around the melt pool in the transverse section. In the thin surface layer which is cooled down by convection, the solidification starts from the surface and the grains grow towards the center along the direction normal to the surface which is the y direction in our geometry. Hence, the thermal gradient compo-



(a) Solidification map of Inconel 718 [36].



(b) Schematic view of thermal flux around the melt pool.

Figure 4: Solidification map of Inconel 718 explaining the observed microstructure: columnar grains in the inner part of the wall; equiaxed grains near the surface due to convection which changes solidification conditions.

ment that is going to be considered to study solidification in this area is the y component: $G_{out} \approx g_y$.

A simplified thermal analysis is conducted to evaluate the y component on the thermal gradient, using material coefficients given in Tab. 1. In this table, the material parameters for Inconel 718 are taken from [26] and the convection coefficient h is chosen as a compromise value between high convection below the nozzle and low convection far from it [7, 21, 39].

It is assumed that, on the frontier located at 0.080mm depth between small equiaxed grains near the surface and large columnar grains in the inner part, the conduction flux in the small grains region near the surface with thickness p is directed along y direction and is equal to the convection flux at the surface:

$$\frac{k}{p} (T_m - T_s) = h (T_s - T_{ext}) \quad (4)$$

where k denotes the thermal conductivity, h the convection coefficient, T_m the melting temperature, T_s the surface temperature and T_{ext} the external temperature. Eq. 4 enables the derivation of T_s . The y component of thermal gradient that drives the solidification near the surface G_{out} can be estimated using a linear approximation:

$$G_{out} \approx g_y \approx \frac{T_m - T_s}{p} \quad (5)$$

$$G_{out} \approx \frac{h}{hp + k} (T_m - T_{ext}) \approx \frac{h}{k} (T_m - T_{ext}) \quad (6)$$

since $hp \ll k$. It follows that $G_{out} \approx 2.10^3$ K/m.

The interface velocity denoted R can be derived from $R = \dot{T}/G$ where \dot{T} is the cooling speed [37]. Let us now compare \dot{T}_{out} and \dot{T}_{in} , the cooling speeds, respectively at the surface and in the kernel of the wall.

Using the material coefficients in Tab. 1, the characteristic time of convection $\tau_{conv} = ec\rho/2h$ [40] and the characteristic time of conduction $\tau_{cond} = eL/D = \rho ceL/k$ [41] are derived. This implies that $\tau_{conv} \approx 4 \tau_{cond}$. As a consequence from this ratio, $\dot{T}_{out} \approx 1/4 \dot{T}_{in}$. Furthermore, the order of magnitude of the thermal gradients G_{out} and G_{in} approximated previously provides $G_{out} \approx 1/1000 G_{in}$. Hence, an estimation of the relative magnitudes of R_{out} and R_{in} is given by $R_{out} \approx 250 R_{in}$. Finally, this evaluation enables to locate (R_{out}, G_{out}) in the equiaxed region in the solidification map of Fig. 4a. This is consistent with the experimental observations showing a thin layer of equiaxed grains at the surface.

Let us remark that the solidification map could not directly be used to provide complementary rationale to the mechanisms described in Fig. 3 regarding dwell time. Indeed, this maps describe solidification for monotonic cooling and cannot account for additional heating and remelting.

The previous values for G and R are only rough estimations with a high uncertainty. However, the above analysis provides only orders of magnitude of G and R . Since the position of the points in the log-log solidifi-

Material coefficients			
Thermal conductivity	k	21	$\text{W.m}^{-1}.\text{K}^{-1}$
Convection coefficient	h	30	$\text{W.m}^{-2}.\text{K}^{-1}$
Thermal capacity	c	435	$\text{J.kg}^{-1}.\text{K}^{-1}$
Thermal diffusivity	$D = c\rho/k$	5.89e-6	$\text{m}^2.\text{s}^{-1}$
Density	ρ	8190	kg.m^{-3}
Melting temperature (solidus)	T_m	1260	$^{\circ}\text{C}$
External temperature	T_{ext}	20	$^{\circ}\text{C}$
Geometry			
Plate length	L	90	mm
Plate height	a	20	mm
Plate thickness	e	0.80	mm
Layer thickness	Δz	0.2	mm

Table 1: Thermal and convection coefficients of Inconel 718 [21, 26] and geometric characteristics of the sample.

cation map are far from the boundaries of the domains, one can qualitatively justify the varying microstructure along the thickness depth of the wall. More precise evaluations of thermal gradients, cooling rates and melt pool shapes could be carried out using high-fidelity thermal simulations [42] to support the qualitative analysis presented here.

5. Conclusion

This study has highlighted that dwell time is a key parameter of Laser Cladding process with a strong impact on the microstructure of the deposit. Moreover, within the process parameters, it is easier to tune dwell time as laser speed and power or powder flow rate modifications impact the bead shape that needs to fulfill geometrical requirements to ensure material health. Consequently, interlayer dwell time should be used to optimize the repair process lasing strategy in order to get a desired microstructure.

As a perspective of this work, in-situ tensile tests will be carried out to investigate the mechanical behavior of those different microstructure gradients and characterize the induced strain localization at the grain level. We expect to get elements to choose an optimized microstructure depending on the targeted behavior.

Finally, it can be argued that adding a dwell time to the process increases manufacturing time and cost and is not a viable industrial option. However, when repair is considered, the volume fraction of clad material is small. Increasing the duration of the repair process is not penalizing when compared to the replacement cost then not an issue compared to the cost of complex components that can be repaired. As a final conclusion, the

choice of an appropriate dwell time depends both on material microstructural constraints and on global manufacturing choices.

Acknowledgment

The authors would like to thank Guillaume Marion from *Safran Additive Manufacturing* for fruitful discussions and *Direction Général de l'Armement (DGA)* for the funding of the *BeAM Mobile* machine with which the clad samples were manufactured. The FEG SEM FEI Quanta 600 has been acquired with the financial support of Region Ile-de-France (SESAME 2004 program), CNRS, and Ecole Polytechnique.

- [1] J. Michael Wilson, Cecil Piya, Yung C. Shin, Fu Zhao, and Karthik Ramani. Remanufacturing of turbine blades by laser direct deposition with its energy and environmental impact analysis. *Journal of Cleaner Production*, 80:170 – 178, 2014.
- [2] Benjamin Graf, Andrey Gumenyuk, and Michael Rethmeier. Laser metal deposition as repair technology for stainless steel and titanium alloys. *Physics Procedia*, 39:376 – 381, 2012. Laser Assisted Net shape Engineering 7 (LANE 2012).
- [3] T. DebRoy, H.L. Wei, J.S. Zuback, T. Mukherjee, J.W. Elmer, J.O. Milewski, A.M. Beese, A. Wilson-Heid, A. De, and W. Zhang. Additive manufacturing of metallic components – Process, structure and properties. *Progress in Materials Science*, 92:112 – 224, 2018.
- [4] Wook Jin Oh, Wook Jin Lee, Min Seob Kim, Jong Bae Jeon, and Do Sik Shim. Repairing additive-manufactured 316L stainless steel using direct energy deposition. *Optics & Laser Technology*, 117:6–17, 2019.
- [5] P.L. Blackwell. The mechanical and microstructural characteristics of laser-deposited Inconel 718. *Journal of Materials Processing Technology*, 170(1):240 – 246, 2005.
- [6] H. Paydas, A. Mertens, R. Carrus, J. Lecomte-Beckers, and J. Tchoufang Tchoundjang. Laser cladding as repair technology for Ti-6Al-4V alloy: Influence of building strategy on microstructure and hardness. *Materials & Design*, 85:497 – 510, 2015.

- [7] M. Biegler, B. Graf, and M. Rethmeier. In-situ distortions in lmd additive manufacturing walls can be measured with digital image correlation and predicted using numerical simulations. *Additive Manufacturing*, 20:101 – 110, 2018.
- [8] Yangyang Lei, Jun Xiong, and Rong Li. Effect of inter layer idle time on thermal behavior for multi-layer single-pass thin-walled parts in GMAW-based additive manufacturing. *The International Journal of Advanced Manufacturing Technology*, 96(1):1355–1365, Apr 2018.
- [9] Y. Yang, M.F. Knol, F. van Keulen, and C. Ayas. A semi-analytical thermal modelling approach for selective laser melting. *Additive Manufacturing*, 21:284 – 297, 2018.
- [10] Jichang Liu and Lijun Li. Effects of process variables on laser direct formation of thin wall. *Optics & Laser Technology*, 39(2):231 – 236, 2007.
- [11] V. Ocelik, I. Furar, and J.Th.M. De Hosson. Microstructure and properties of laser clad coatings studied by orientation imaging microscopy. *Acta Materialia*, 58(20):6763 – 6772, 2010.
- [12] Lakshmi L. Parimi, Ravi G. A., Daniel Clark, and Moataz M. Attallah. Microstructural and texture development in direct laser fabricated Inconel 718. *Materials Characterization*, 89:102 – 111, 2014.
- [13] Zhuqing Wang, Todd A. Palmer, and Allison M. Beese. Effect of processing parameters on microstructure and tensile properties of austenitic stainless steel 304L made by directed energy deposition additive manufacturing. *Acta Materialia*, 110:226 – 235, 2016.
- [14] Kangbo Yuan, Weiguo Guo, Penghui Li, Jianjun Wang, Yu Su, Xin Lin, and Yanping Li. Influence of process parameters and heat treatments on the microstructures and dynamic mechanical behaviors of Inconel 718 superalloy manufactured by laser metal deposition. *Materials Science and Engineering: A*, 721:215 – 225, 2018.
- [15] G.P. Dinda, A.K. Dasgupta, and J. Mazumder. Texture control during laser deposition of nickel-based superalloy. *Scripta Materialia*, 67(5):503 – 506, 2012.
- [16] Carolin Körner, Harald Helmer, Andreas Bauereiß, and Robert Singer. Tailoring the grain structure of IN718 during selective electron beam melting. *MATEC Web of Conferences*, 14:08001, 01 2014.
- [17] J. Mazumder H. L. Wei and T. DebRoy. Evolution of solidification texture during additive manufacturing. *Nature*, 2015.
- [18] Haider Ali, Hassan Ghadbeigi, and Kamran Mumtaz. Effect of scanning strategies on residual stress and mechanical properties of selective laser melted ti6al4v. *Materials Science and Engineering: A*, 712:175 – 187, 2018.
- [19] H.Y. Wan, Z.J. Zhou, C.P. Li, G.F. Chen, and G.P. Zhang. Effect of scanning strategy on mechanical properties of selective laser melted inconel 718. *Materials Science and Engineering: A*, 753:42 – 48, 2019.
- [20] Tien T. Roehling, Sheldon S.Q. Wu, Saad A. Khairallah, John D. Roehling, S. Stefan Soezeri, Michael F. Crumb, and Manyalibo J. Matthews. Modulating laser intensity profile ellipticity for microstructural control during metal additive manufacturing. *Acta Materialia*, 128:197 – 206, 2017.
- [21] J.C. Heigel, P. Michaleris, and E.W. Reutzel. Thermo-mechanical model development and validation of directed energy deposition additive manufacturing of Ti–6Al–4V. *Additive Manufacturing*, 5:9 – 19, 2015.
- [22] B. K. Foster, A. M. Beese, J. S. Keist, E. T. McHale, and T. A. Palmer. Impact of interlayer dwell time on microstructure and mechanical properties of nickel and titanium alloys. *Metallurgical and Materials Transactions A*, 48(9):4411–4422, Sep 2017.
- [23] Nathan A. Kistler, David J. Corbin, Abdalla R. Nassar, Edward W. Reutzel, and Allison M. Beese. Effect of processing conditions on the microstructure, porosity, and mechanical properties of Ti-6Al-4V repair fabricated by directed energy deposition. *Journal of Materials Processing Technology*, 264:172 – 181, 2019.
- [24] Yanis Balit, Eric Charkaluk, and Andrei Constantinescu. Digital image correlation for microstructural analysis of deformation pattern in additively manufactured 316L thin walls. *Additive Manufacturing*, 2019.
- [25] Yanis Balit, Camille Guévenoux, Manas V. Upadhyay, Eric Charkaluk, and Andrei Constantinescu. Digital image correlation for microstructural localisation analysis of SS316L repaired by directed energy deposition. *Submitted to Material Letters*, 2020.
- [26] Special Metals. Inconel alloy 718, 2018.
- [27] ARCAM. Metal powders. <http://www.arcam.com/technology/products/metal-powders/>, 2019.
- [28] BeAM. Gamme de Machines - MOBILE et MODULO. <http://www.beam-machines.fr/fr/produits>, 2016.
- [29] W. Kurz and D.J. Fisher. *Fundamentals of Solidification*. 4th edition, CRC Press, 1998.
- [30] O. Nenaïd, V. Ocelik, and J. Th. M. De Hosson. Texture development in direct powder deposition. *Journal of Laser Applications*, 2017.
- [31] Johannes A. Koepf, Martin R. Gotterbarm, Matthias Markl, and Carolin Körner. 3D multi-layer grain structure simulation of powder bed fusion additive manufacturing. *Acta Materialia*, 152:119 – 126, 2018.
- [32] Fencheng Liu, Xin Lin, Han Leng, Jun Cao, Qiang Liu, Chunping Huang, and Weidong Huang. Microstructural changes in a laser solid forming Inconel 718 superalloy thin wall in the deposition direction. *Optics & Laser Technology*, 45:330 – 335, 2013.
- [33] Josefine Svenungsson, Isabelle Choquet, and Alexander F.H. Kaplan. Laser welding process – a review of keyhole welding modelling. *Physics Procedia*, 78:182 – 191, 2015. 15th Nordic Laser Materials Processing Conference, Nolamp 15.
- [34] Chong Teng, Deepankar Pal, Haijun Gong, Kai Zeng, Kevin Briggs, Nachiket Patil, and Brent Stucker. A review of defect modeling in laser material processing. *Additive Manufacturing*, 14:137 – 147, 2017.
- [35] V. Gunenthiram, P. Peyre, M. Schneider, M. Dal, F. Coste, I. Koutiri, and R. Fabbro. Experimental analysis of spatter generation and melt-pool behavior during the powder bed laser beam melting process. *Journal of Materials Processing Technology*, 251:376 – 386, 2018.
- [36] Huiliang Wei, Tuhin Mukherjee, and Tarasankar Debroy. Grain growth modeling for additive manufacturing of nickel based alloys. *6th International Conference on Recrystallization and Grain Growth*, 07 2016.
- [37] Joy Gockel, Nathan Klingbeil, and Srikanth Bontha. A closed-form solution for the effect of free edges on melt pool geometry and solidification microstructure in additive manufacturing of thin-wall geometries. *Metallurgical and Materials Transactions B*, 47(2):1400–1408, Apr 2016.
- [38] Xiao Ding, Yuichiro Koizumi, Daixiu Wei, and Akihiko Chiba. Effect of process parameters on melt pool geometry and microstructure development for electron beam melting of in718: A systematic single bead analysis study. *Additive Manufacturing*, 26:215–226, 2019.
- [39] Panagiotis Michaleris. Modeling metal deposition in heat transfer analyses of additive manufacturing processes. *Finite Elements in Analysis and Design*, 86:51 – 60, 2014.
- [40] Hervé Louche and André Chrysochoos. Thermal and dissipative effects accompanying liders band propagation. *Materials Science and Engineering: A*, 307(1):15 – 22, 2001.

- [41] E. Marin. Characteristic dimensions for heat transfer. *Lat. Am. J. Phys. Educ.*, 2010.
- [42] Zhaorui Yan, Weiwei Liu, Zijue Tang, Xuyang Liu, Nan Zhang, Mingzheng Li, and Hongchao Zhang. Review on thermal analysis in laser-based additive manufacturing. *Optics & Laser Technology*, 106:427 – 441, 2018.